



Study on the off situ reconstruction of the core neutron field based on dual-task hybrid network architecture

Pei Cao¹ · Hui Ding¹ · Cheng-Long Cao² · Zi-Hui Yang³ · Guo-Min Sun³

Received: 28 September 2023 / Revised: 19 March 2024 / Accepted: 1 April 2024 / Published online: 18 December 2024

© The Author(s), under exclusive licence to China Science Publishing & Media Ltd. (Science Press), Shanghai Institute of Applied Physics, the Chinese Academy of Sciences, Chinese Nuclear Society 2024

Abstract

The off situ accurate reconstruction of the core neutron field is an important step in realizing real-time reactor monitoring. The existing off situ reconstruction method of the neutron field is only applicable to cases wherein a single region changes at a specified location of the core. However, when the neutron field changes are complex, the accurate identification of the individual changed regions becomes challenging, which seriously affects the accuracy and stability of the neutron field reconstruction. Therefore, this study proposed a dual-task hybrid network architecture (DTHNet) for off situ reconstruction of the core neutron field, which trained the outermost assembly reconstruction task and the core reconstruction task jointly such that the former could assist the latter in the reconstruction of the core neutron field under core complex changes. Furthermore, to exploit the characteristics of the ex-core detection signals, this study designed a global-local feature upsampling module that efficiently distributed the ex-core detection signals to each reconstruction unit to improve the accuracy and stability of reconstruction. Reconstruction experiments were performed on the simulation datasets of the CLEAR-I reactor to verify the accuracy and stability of the proposed method. The results showed that when the location uncertainty of a single region did not exceed nine and the number of multiple changed regions did not exceed five. Further, the reconstructed ARD was within 2%, RD_{max} was maintained within 17.5%, and the number of $RD_{\geq 10\%}$ was maintained within 10. Furthermore, when the noise interference of the ex-core detection signals was within $\pm 2\%$, although the average number of $RD_{\geq 10\%}$ increased to 16, the average ARD was still within in 2%, and the average RD_{max} was within 22%. Collectively, these results show that, theoretically, the DTHNet can accurately and stably reconstruct most of the neutron field under certain complex core changes.

Keywords Real-time reactor monitoring · Core neutron field reconstruction · Dual-task hybrid network architecture · Global-local feature upsampling module

1 Introduction

Nuclear energy is a strategic energy source that is safe, efficient, has low-carbon emission, and has high energy density. It has become an important part of the world energy system in recent years [1]. A reactor is a device that releases nuclear energy in a controlled manner and converts it into heat energy. Thus, its safe and effective operation has been of concern to the industry and the public. A real-time reactor monitoring system is an important safeguard to ensure the safety and economy of a reactor, which primarily monitors the core power, temperature, neutron distribution, and other physical quantities. Among these physical quantities, the in-core neutron distribution (called the core neutron field) provides basic data for reactor power distribution and burn-up calculations, material irradiation damage analysis, and other

This work was supported by the National Natural Science Foundation of China (No.12305344) and the 2023 Anhui university research project of China (No.2023AH052179).

✉ Pei Cao
caopei@hfu.edu.cn

¹ School of Artificial Intelligence and Big Data, Hefei University, Hefei 230001, China

² College of Electronic Engineering, National University of Defense Technology, Hefei 230001, China

³ Institute of Nuclear Energy Safety Technology, HFIPS, Chinese Academy of Sciences, Hefei 230027, China

studies. Therefore, the accurate acquisition of the neutron field is an important task in reactor monitoring systems.

Direct acquisition uses in-core detection signals to reconstruct a neutron field. In recent years, researchers have proposed various in situ reconstruction methods, such as neutron detector-based methods [2–5] and non-neutron detector-based methods [6, 7], which have achieved good reconstruction results in pressurized- and heavy-water reactors. However, an advanced reactor core has a harsh operating environment, such as high temperature [8], strong magnetic field [9], and modularity [10–12]. Thus, it is difficult to install neutron-monitoring instruments in the core, which greatly affects detector signal acquisition. Ultimately, this affects the accuracy and stability of the in-situ reconstruction methods. Because ex-core detectors are flexible and unaffected by the harsh environment of the core, core neutron field reconstruction based on ex-core detection signals (namely off situ reconstruction) is the focus of the current research. Specifically, off situ reconstruction methods include analytical reconstruction and neural network methods.

Analytical reconstruction is a formula-driven solution-based method. In 2019, Cao et al. [13] reconstructed the neutron energy spectrum by constructing a response formula for the ex-core detection signals and core neutron spectrum. However, when the neutron field to be reconstructed becomes more complex, there is an ill-posed problem when directly solving it using the response formula. Thus, certain researchers have further developed an analytical reconstruction method based on an iterative optimization algorithm, which has been applied to the reconstruction of gamma radiation fields [14], negative ion beams [15], and reactor power distributions [16, 17]. To reconstruct the neutron field, Rodionov et al. [18] reconstructed DD and DT neutron emissivity profiles in two-dimensional space based on the principle of maximum likelihood estimation. Goricanec et al. [19] deduced a neutron flux redistribution factor based on an ex-core detector and reconstructed the neutron flux distribution under specific working conditions. Although analytical reconstruction methods do not require a large amount of data to solve the core neutron field problem, the accuracy and speed of analytical reconstruction cannot be guaranteed.

In recent years, the neural network reconstruction methods have become a common algorithm for off situ reconstruction of core physical quantities, such as reactor power distribution reconstruction [20, 21], fast neutron direction reconstruction [22], fault diagnosis [23, 24], multi-nuclide source term estimation [25], reactor temperature distribution reconstruction [26], source term distribution reconstruction [27, 28], and fusion plasma prediction [29, 30], etc. They exhibit a strong generalization ability and can perform physical quantity reconstruction under a variety of core changes. However, these algorithms focus only on

the spatial distribution of physical quantities and cannot satisfy the requirements of high-dimensional neutron field reconstruction. To realize the reconstruction of the neutron distribution with space and energy, Cao et al. [31, 32] developed a neutron field reconstruction method based on a shallow neural network, and the neutron distribution with two-dimensional space and energy was successively reconstructed on the reactor models of a pressurized water reactor and lead-based reactor. Further, Cao et al. [33] developed a pipeline architecture based on a deep neural network for complex neutron field reconstruction. This pipeline architecture trains the core changed region recognition, core relay region reconstruction, and core neutron field reconstruction separately, which are then performed sequentially to achieve the reconstruction of the 3D neutron field. However, this method is applicable to cases wherein only a single region changes at a specified location of the core. In fact, the location and number of core-changed regions are uncertain, and this situation can seriously affect the accuracy and stability of neutron field reconstruction.

To address this limitation, this study proposed a joint training model based on a hybrid architecture. The architecture simultaneously trains the core relay reconstruction and core neutron field reconstruction subtasks. Simultaneously, the relay region reconstruction task was used to assist the core neutron field reconstruction task to improve the accuracy of the neutron field reconstruction. Based on the above study, the core neutron field reconstruction can still be realized in the case of unknown core-changed region information.

2 Related work

2.1 Multi-task deep learning

Multitask deep learning (MTDL) [34] is a model training paradigm wherein the main idea involves training with multiple tasks simultaneously using shared representations to learn information between related tasks. Shared representations can improve the efficiency of data feature extraction, improve the learning speed of related tasks, and alleviate the weaknesses of deep learning, such as large data scale and time consumption. Zhao et al. [35] introduced a classification method that divides MTDL architectures into four types: cascaded, parallel, interactive, and hybrid.

Figure 1a presents a typical cascaded architecture. This architecture does not have a shared task layer and the output of the previous task is fed directly to the subsequent training task. The cascaded approach is primarily suitable for cases wherein the subsequent task relies heavily on the output of the former task. Thus, the results of the former task

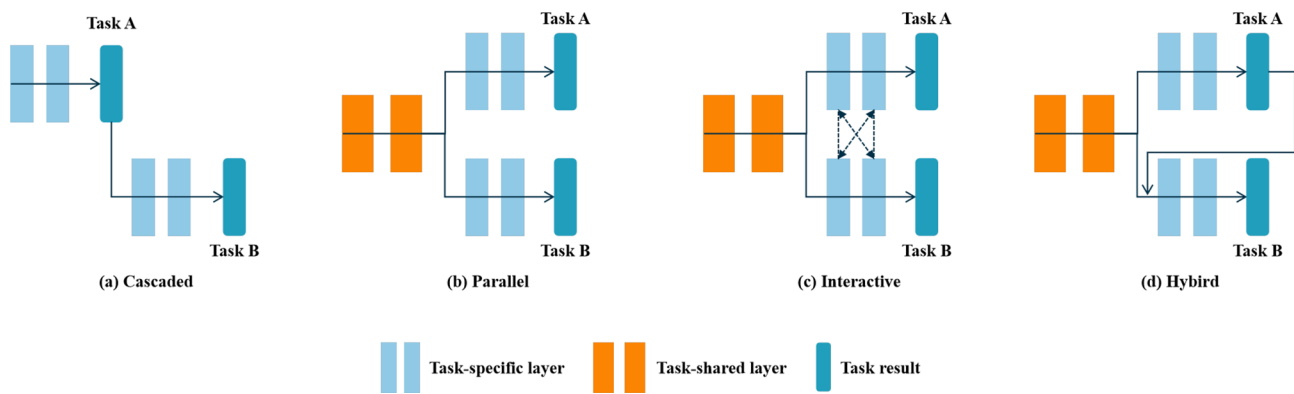


Fig. 1 (Color online) Schematic of four multi-task deep learning architectures [35]: **a** cascaded architecture, **b** parallel architecture, **c** interactive architecture, and **d** hybrid architecture

significantly affect the performance of the subsequent task in the task combination.

Figure 1b presents a typical parallel architecture. In this architecture, a partially shared representation layer exists and different tasks are computed in parallel on specific task networks. This parallel approach may be more suitable for addressing task combinations that are related but exhibit different levels of complexity. Examples include the image segmentation and image generation tasks.

An interactive architecture refers to the presence of one or more connections between task-specific layers, which enables the exploration of deep correlations between tasks, as illustrated in Fig. 1c. It is more suitable for solving situations wherein there is a significant correlation between multiple tasks, and can enable related tasks to provide useful auxiliary information.

Owing to the diversity of detailed network structures, researchers have defined the fourth category as a hybrid architecture (Fig. 1d). Typically, in a hybrid architecture, at least two of the following strategies are used: cascaded, parallel, or interactive. The hybrid architecture can fully leverage the advantages of the three architectures and is well suited for complex task combinations.

Core neutron field data exhibit the characteristics of high-dimensional and large-scale data, and there are certain correlations among the multiple tasks involved in core reconstruction. Therefore, this study applied MDTL to the reconstruction of core neutron fields. Through cooperative learning among different tasks, the aim was to further enhance the efficiency of the core neutron field reconstruction using ex-core detection signals.

2.2 Pipeline reconstruction architecture

The pipeline reconstruction architecture (PRA) proposed by the authors in 2022 [33] is a novel and effective algorithm for studying 3D neutron field [33]. The architecture

ranging from “coarse-grained” to “fine-grained” reconstruction comprises three separate tasks. When all the tasks are trained individually, the core neutron field is sequentially reconstructed.

As shown in Fig. 2, the reconstruction architecture is based on a pipeline pattern. The first stage of the architecture is a core changed-region recognition module, designed by convolutional neural networks. It accurately identifies the core-changed region based on ex-core detection signals. In the second stage, an improved variational autoencoder is designed to reconstruct the core relay region. After determining the core-change region, the neutron field of the relay region is predicted by inputting ex-core detection signals. In the third stage of reconstruction, the neutron field in the relay region is converted from two-dimensions (2D) to three-dimensions (3D), and then the distribution of the 3D core neutron field is predicted using the 3D full convolution-based reconstruction module. By sequentially executing these three modules, the pipeline-based architecture enables the reconstruction of the 3D core neutron field.

Notably, the PRA must identify the location of a single-core changed region. However, the location and number of core-changed regions are generally uncertain. Therefore, this architecture has certain limitations.

3 Dual-task hybrid network architecture

This study proposed a dual-task hybrid network architecture (DTHNet), which is illustrated in Fig. 3. The ex-core detector signals were first subjected to image processing to form the required data structure for the model. Subsequently, the processed data were fed into a dual-task shared global-local feature upsampling module. Through nonlinear transformations, the features carried by the ex-core detector signals were allocated to each unit to be reconstructed. The hidden

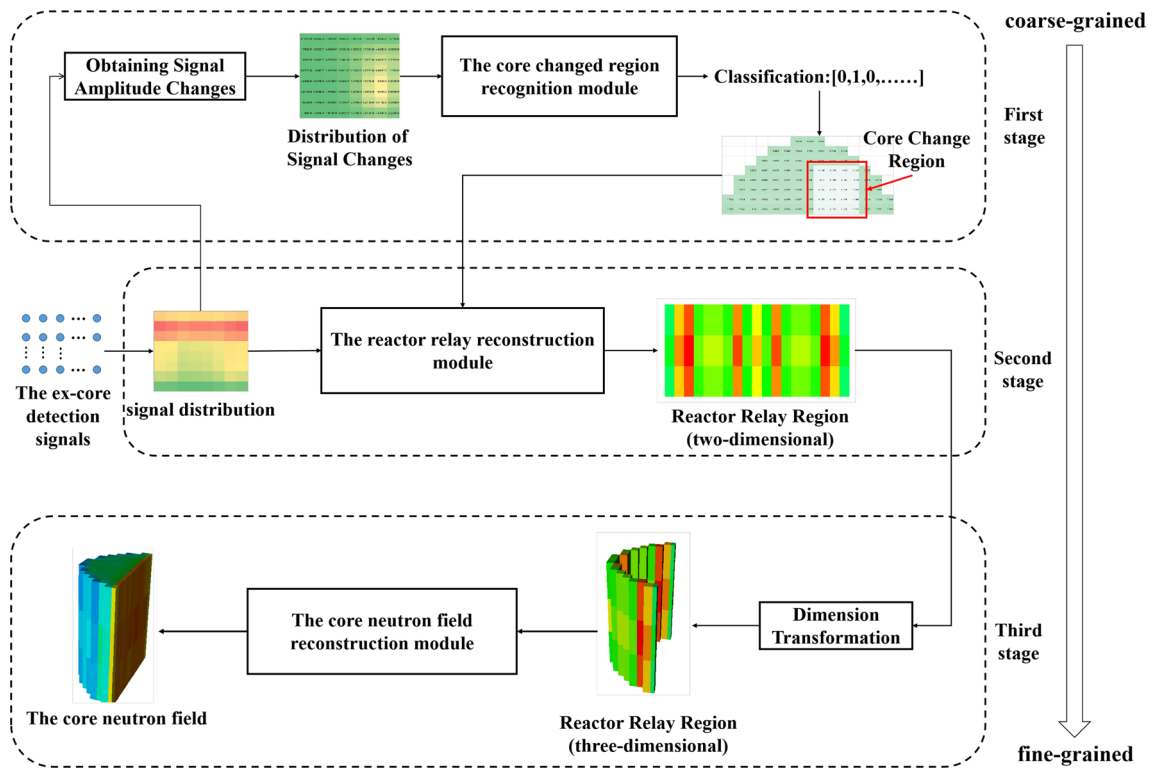


Fig. 2 (Color online) Reconstruction architecture based on a pipeline pattern. This architecture comprises three main modules: the core changed region recognition, reactor relay reconstruction, and core neutron field reconstruction modules

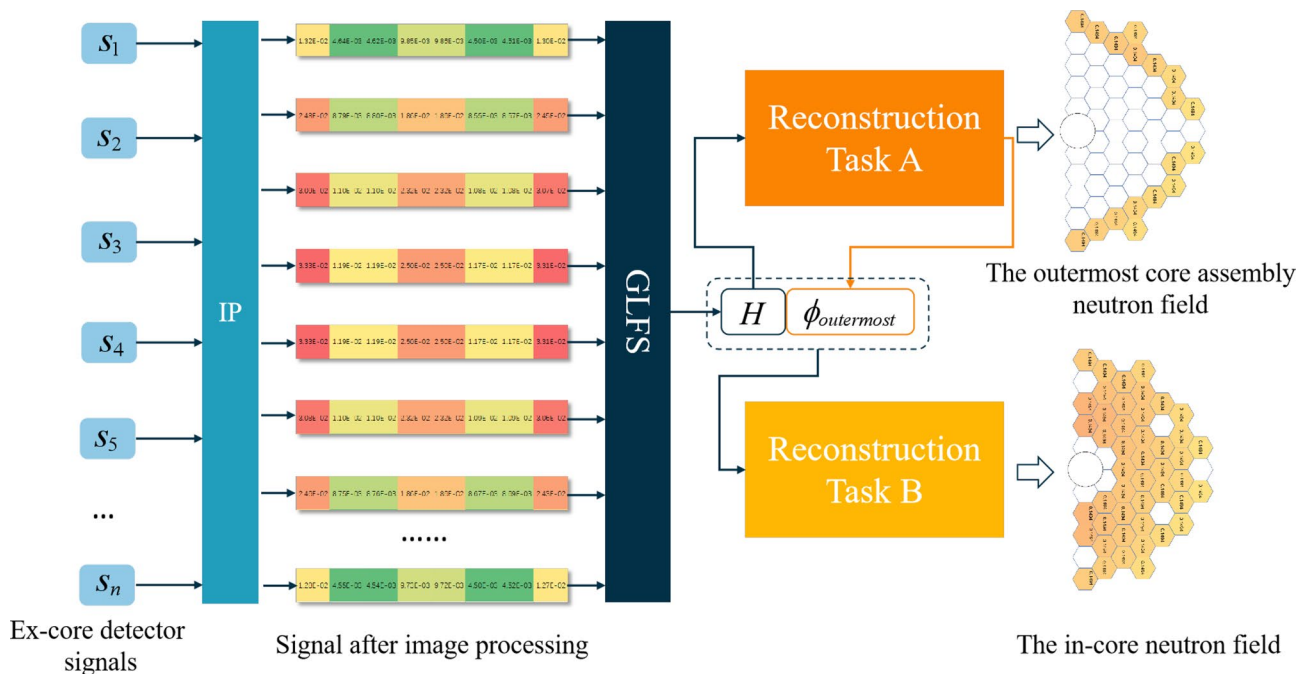


Fig. 3 (Color online) Dual-task hybrid network architecture. The framework comprises three main parts: image processing (IP), global-local feature upsampling module (GLFS), and reconstruction tasks.

Task A is for reconstructing the neutron field of outermost core assemblies and Task B is for reconstructing the core neutron field

vectors H_{GLFS} served as inputs for the downstream tasks and continue the training process.

The downstream tasks in this study mainly comprised two tasks: reconstruction of the neutron field in the outermost core assemblies (Task A) and reconstruction of the core neutron field (Task B). Here, Task A was used to assist Task B. The specific reasons are as follows. The outermost core assemblies are the region with a strong response from the ex-core detector, and it is also an unavoidable region for neutrons to be transported from the in-core to the ex-core. Therefore, the outermost core assembly can serve as a relay region where the ex-core detector responds to core neutrons.

However, there was a significant difference in the complexity of the two tasks in terms of data construction. As shown in Fig. 3, the data of the core neutron field was considerably more than that of the neutron field in the outermost core assemblies. According to the applicable scenarios of four architectures of the MTDL, this study proposed a parallel + cascaded dual-task training approach. Although both tasks were trained in parallel, the neutron field in the outermost core assemblies $\phi_{outermost}$ was concatenated with the hidden vectors H_{GLFS} and then used as the input for the reconstruction of the core neutron field.

3.1 Image processing of neutron data

The purpose of image processing is to organize the neutron distribution in the reactor based on the arrangement of image pixels to facilitate efficient feature extraction and transformation by the neural network layer. The reasons for this design are as follows/The core neutron field has strong correlations between adjacent assemblies in 3D space, such as the relationships between pixels in an image. Therefore, each assembly to be reconstructed can be regarded as a pixel, and the number of energy groups corresponds to the number of channels in the image (such as the RGB channels in an image).

Typically, both discrete ex-core detection signals and continuous neutron fields are the objects of image processing. For discrete ex-core detection signals, imaging processing forms a 3D signals tensor according to the spatial position of each detection point. Subsequently the 3D signals are augmented to four-dimensions (4D) by adding the energy dimension to facilitate the extraction and allocation of the ex-core detection signal features through the three-dimensional convolutional network layer. For a continuous core neutron field, image processing discretizes the neutron field from both space and energy to form a 4D tensor (energy, height, weight, and length); where, height is the height after discretization of a neutron field in the core, weight is the discretized width of the neutron field in the core, length is the discretized length of the neutron field in the core, and energy is the number of discretized energy groups.

According to the above design, the sample after image processing includes the following steps.

$$S = \{s, (\phi)_{coreEdge}^{E \times H \times W \times L}, (\phi)_{core}^{E \times H \times W \times L}\} \quad (1)$$

where s represents the ex-core detection signals, $(\phi)_{coreEdge}$ represents the neutron field of the outermost core assemblies, $(\phi)_{core}$ represents the core neutron field, and $E \times H \times W \times L$ is the sample size, which represents the number of reconstruction units. In the study, the number of energy groups was used as the convolutional depth. In addition, the magnitude of the neutron field distribution values calculated by the Monte Carlo method is small, which is not conducive to model training. Therefore, this study adopted normalization processing to limit the magnitude of the neutron field to the range of [0,1].

3.2 Global-local feature upsampling module

For a multitask architecture, it is essential to extract the shared features of tasks. By upsampling the features contained in the ex-core detection signals, the features carried by the signals can be evenly distributed to each reconstruction unit. Owing to the large magnitude difference between the values of the core neutron field, it is difficult to assign features to certain reconstruction units, and the model cannot reconstruct units with small numerical values.

Therefore, a global-local feature upsampling module was designed in this study. The architecture diagram of the module is shown in Fig. 4. The module was divided into two parts to upsample the information carried by the ex-core detection signals. The first was the global feature upsampling network, which ensured that the ex-core detection signals covered every reconstruction unit, and the network output was H_{Global} . The second was a local feature upsampling network, which was primarily used to assign features to energy groups with less neutron distribution. The network output was H_{Local} . Finally, the sampling results of the two parts were concatenated as inputs for the following two reconstruction tasks.

3.3 Dual-task optimization function

The hidden layer vector H_{GLFS} obtained from the global-local feature upsampling module was used to train the reconstruction task of the neutron field in the outermost core assemblies and that of the core neutron field. The formula for the reconstruction of the neutron field in the outermost core assemblies is as follows:

$$L_A = \frac{1}{N} \sum_{j=1}^N (f_A^j(H_{GLFS}) - \phi_A^j)^2 \quad (2)$$

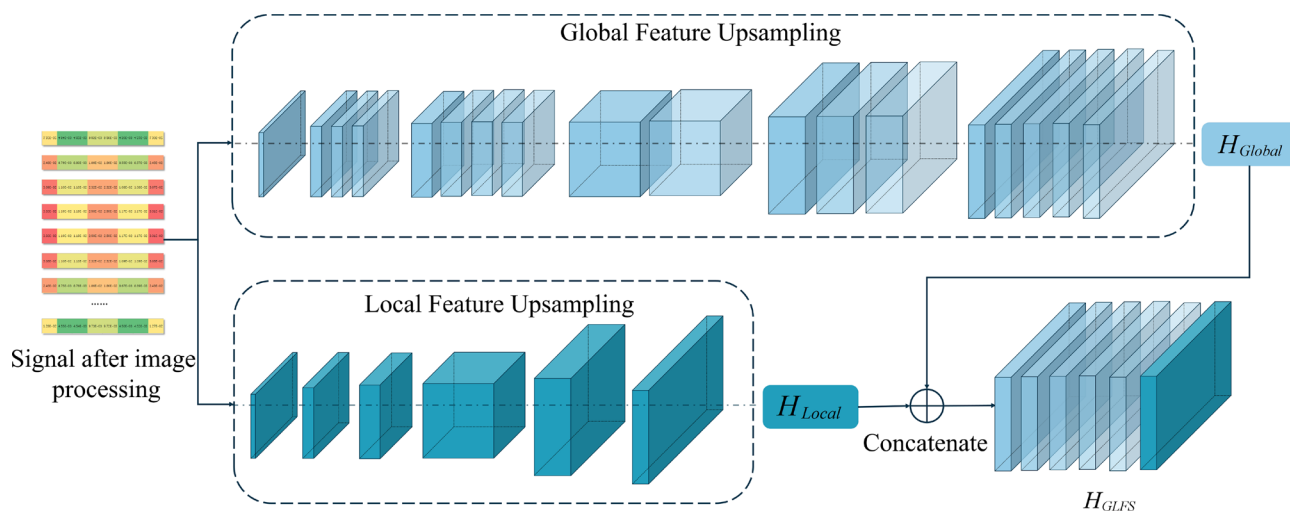


Fig. 4 (Color online) Global-local feature upsampling module. Both global and local sub-modules upsample ex-core signals. Finally, the outputs of sub-module are concatenated together as inputs for downstream tasks

where $N = E \times H \times C_A$, E is the number of discretized energy groups, H is the height of the core neutron field, and $C_A = \sum_{i=1}^W n_i$, where W is the width of the core neutron field, n_i is the number of outermost core assemblies in the i -th line. Further, H_{GLFS} is the output vector of GLFS module, $f_A^j(H_{GLFS})$ represents the reconstructed data of the j -th outermost core assemblies, and ϕ_A^j represents the reference data of the j -th outermost core assemblies obtained through Monte Carlo simulations.

Subsequently, the results of the outermost core assemblies were concatenated to the hidden layer vectors to obtain new hidden layer vectors that were used for core neutron field reconstruction training. This step is similar to a residual network, which not only retains the original sampled features but also incorporates certain learned knowledge features, thereby improving the effectiveness of core neutron field reconstruction. Therefore, the loss function for the second task is as follows:

$$L_B = \frac{1}{M} \sum_{j=1}^M (f_B^j(H_{GLFS}) - \phi_B^j)^2 \quad (3)$$

where $M = E \times H \times C_B$, E is the number of discretized energy groups, H is the height of the core neutron field, and $C_B = \sum_{i=1}^W l_i$, where W is the width of the core neutron field, l_i is the number of core assemblies in the i -th line of width. Further, H_{GLFS} is the output vector of GLFS module, $f_B^j(H_{GLFS})$ represents the reconstructed data of the j -th-core assemblies, and ϕ_B^j represents the reference data of the j -th-core assemblies obtained through Monte Carlo simulations.

Finally, the loss function of the entire model training comprised L_A and L_B . The formula is as follows:

$$L_{DTHNet} = \lambda * L_A + \beta * L_B \quad (4)$$

where λ and β are hyperparameters. They are used to balance the two tasks during the training of the neural network, and their values are in the range $[0,1]$. Typically, after multiple manual attempts, an appropriate value can be selected to obtain better model learning efficiency.

4 Experimental settings

4.1 Benchmark and dataset

Lead-cooled fast reactors, recommended as fourth-generation nuclear energy systems, have made significant progress in their development. The China Lead-based Experimental Advanced Reactor-I (CLEAR-I) [36] is a lead-cooled fast reactor that operates in both critical and accelerator-driven subcritical modes. The numbers of core assemblies and material summaries are listed in Table 1. As shown in Fig. 5, the CLEAR-I core adopts the commonly used hexagonal prism assemblies of fast reactors. According to the different functions of the assemblies, the core was divided into target, buffer, active, reflecting, and shielding regions from the inside to the outside. The buffer region comprised six assemblies, and the core active region consisted of 94 assemblies, including 86 fuel assemblies (52 of which were replaced with reflector assemblies when the reactor was in subcritical operation) and eight control-rod assemblies.

In this study, the critical mode was selected as the simulated operation mode of the reactor to verify the reconstruction of the neutron field under transient changes in the core. In addition, to reduce the time required for model training,

Table 1 Quantity and material composition of CLEAR-I core components

| Core components | Numbers | Material composition |
|---|---------|--|
| Buffer region | 8 | Lead |
| Fuel assemblies | 86 | UO ₂ with 19.75% enrichment |
| Reflector assemblies | 84 | Lead |
| Shielding assemblies | 48 | Lead, boron |
| Safety rod/control rod/compensatory rod | 3/3/2 | Stainless steel, boron, and cadmium |

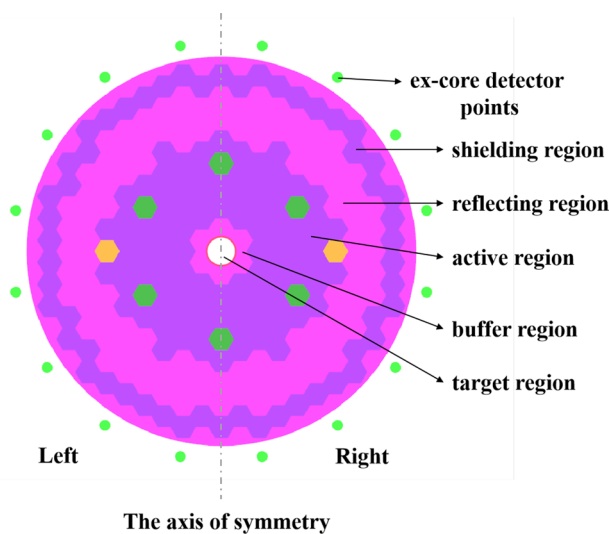


Fig. 5 (Color online) Radial profile of the CLEAR-I reactor

half of the reactor model was selected for verification of the reconstruction method.

According to the characteristics of the neutron distribution in fast reactors, the energy groups for neutron field reconstruction in this study were set as follows: $[0, 1.00 \times 10^{-2}]$ MeV, $[1.00 \times 10^{-2}, 1.00 \times 10^{-1}]$ MeV, $[1.00 \times 10^{-1}, 5.00 \times 10^{-1}]$ MeV, $[5.00 \times 10^{-1}, 1.00]$ MeV, and $[1.00, 2.00 \times 10^1]$ MeV. Figure 6 shows the ex-core detection points and relay region for CLEAR-I model in this study. Herein, 8×8 detection points were set outside the shielding layer; thus, the ex-core detection signals were $s^{8 \times 8}$, and the detection signals were $s^{1 \times 8 \times 1 \times 8}$ after image processing. In addition, the core assembly region was divided into two parts according to the material distribution; thus, the height of the core was 2. Based on the radial profile of the reactor (Fig. 7), the core had a length of 11 and a width of 7. Therefore, in this case, the size of the neutron flux distribution for the outermost assemblies (relay region) of the core was $5 \times 2 \times 18$ and that after image processing was $5 \times 2 \times 7 \times 11$. The dimensions of the neutron field core were $5 \times 2 \times 7 \times 11$.

In line with the symmetry of the model, a Monte Carlo fixed-source calculation was conducted in this study, and the response matrix of the ex-core detection points was obtained. In this study, assembly was used as the basic spatial unit for reconstruction. When the neutron distribution of an assembly changes, the neutron fields of the surrounding assemblies may be affected. Thus, 5–6 adjacent assemblies were chosen as changed regions. In this context, this study set 18 regions where the core changes, and the upper and lower layers of the core contained nine changes.

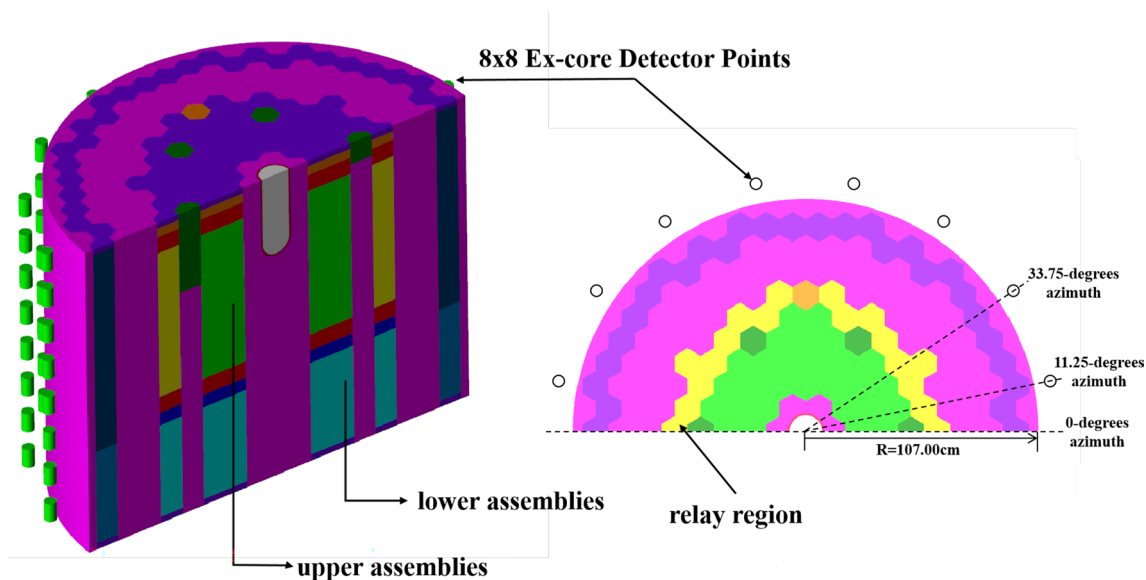


Fig. 6 (Color online) Settings of ex-core detection points and relay region. The relay region is composed of the outermost assemblies of the core

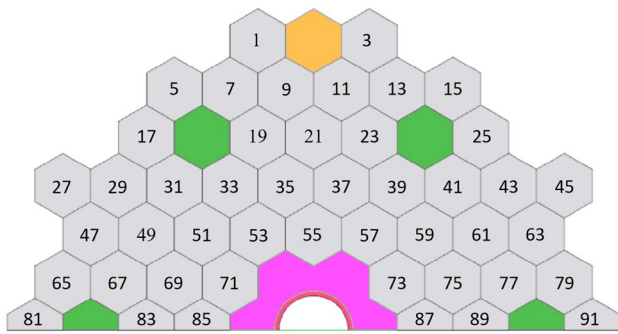


Fig. 7 (Color online) Core assembly cross sections and their serial number (upper layer)

Table 2 Assembly serial numbers corresponding to the regions where the core changes

| Region number | Assembly serial numbers |
|---------------|----------------------------|
| 1 | 49, 51, 67, 69, 71, 83, 85 |
| 2 | 31, 33, 49, 51, 53, 69, 71 |
| 3 | 19, 21, 33, 35, 37, 53, 55 |
| 4 | 21, 23, 35, 37, 39, 55, 57 |
| 5 | 23, 25, 37, 39, 41, 57, 59 |
| 6 | 39, 41, 57, 59, 61, 73, 75 |
| 7 | 59, 61, 73, 75, 77, 87, 89 |
| 8 | 5, 7, 17, 19, 31, 33 |
| 9 | 13, 15, 23, 25, 39, 41 |

the assembly serial numbers of each region of the upper core. The nine regions of the lower core corresponded to the upper core and were not repeated.

In a previous study [21], the authors assumed that only one region of the core was changed at a given time and that the region must be identified first; therefore, a single change dataset (SCD) was constructed. However, in practice, both the location and the number of the changed region are uncertain. Thus, to systematically verify the performance of the architecture proposed in this study, two types of mixed datasets were constructed based on the 18 regions where the core may change: single-region mixed datasets (SRMDs) and multi-region mixed datasets (MRMDs). For SRMDs, the authors assumed that only one region of the core changed at a given time; however, this region was uncertain. In this study, 17 datasets, $SRMDs = \{D_m | 2 \leq m \leq 18\}$, were generated, where m indicates that a single change occurred in one of m certain regions. Thus, m can also be considered the location uncertainty of a single-changed region. For example, when $m = 3$, a region change occurs in regions 3, 4, or 5, and the location uncertainty is 3. For MRMDs, we assumed that there were multiple changed regions at a certain time. Seventeen datasets $MRMDs = \{D_n | 2 \leq n \leq 18\}$

were generated. Further, n represents the number of changed regions in all 18 regions. For example, when $n = 3$, there were 3 certain changed regions in the core, where these 3 regions were randomly selected among the 18 regions. In fact, the magnitude of the core changes in reactor operation was also uncertain; therefore, this study increased the diversity of the neutron field changes; that is, even if any two samples of the training set exhibited a consistently changed region, the magnitude of the change was not consistent. The amplitude of the core-changed region was $0 \sim 15\%$; these datasets are listed in Table 3.

4.2 Hyperparameter settings

Table 4 lists the hyperparameter of DTHNet utilized in the experiment. In the experiment employs a three-dimensional convolutional network layer was employed to reconstruct a four-dimensional core neutron field. Moreover, to preserve the inherent features of the ex-core detection signals, the network architecture in this study did not utilize a pooling layer. Finally, the training parameters of the DTHNet in this study were set to $\lambda = 0.5$, $\beta = 0.1$, epochs = 1500, batch_size = 100.

5 Results and discussion

5.1 Evaluation criteria for neutron field reconstruction

The relative deviation is expressed as RD , where the value quantifies the relative difference between the reconstructed and reference data. Within the context of this study, RD served as an assessment metric for appraising the reconstruction effect of each reconstruction unit within the phase-space neutron field. Meanwhile, the closer ARD is to 0, the smaller the overall difference between the reconstructed data and reference data. The mathematical expression for RD is as follows:

Table 3 Databases and their description

| Database name | Number of datasets | Training data/dataset | Validation data/dataset | Testing data/dataset |
|---------------|--------------------|-----------------------|-------------------------|----------------------|
| SCDs | 18 | 8000 | 2000 | 2000 |
| SRMDs | 17 | 8000 | 2000 | 2000 |
| MRMDs | 17 | 8000 | 2000 | 2000 |

Training data/dataset indicates the amount of data used for training in each dataset. Validation data/dataset represents the amount of data used for validation in each dataset. Testing data/dataset indicates the amount of data used for testing in each dataset

Table 4 Network structure of core neutron field reconstruction based on DTHNet

| Network module | Layer name | Kernel | Strides | Output size |
|---|------------|-----------|-----------|----------------|
| Feature upsampling | InputLayer | – | – | (1, 8, 1, 8) |
| | Conv3DTr | 1 × 2 × 1 | 1 × 2 × 1 | (3, 8, 2, 8) |
| | Conv3DTr | 1 × 2 × 1 | 1 × 2 × 1 | (4, 8, 4, 8) |
| | Conv3DTr | 1 × 2 × 1 | 1 × 2 × 1 | (5, 8, 8, 8) |
| | Conv3DTr | 1 × 1 × 2 | 1 × 1 × 2 | (10, 8, 8, 16) |
| | Conv3D | 2 × 1 × 1 | 2 × 1 × 1 | (10, 4, 8, 16) |
| | Conv3D | 2 × 2 × 1 | 2 × 2 × 1 | (6, 2, 7, 16) |
| | Conv3D | 1 × 1 × 6 | 1 × 1 × 1 | (5, 2, 7, 11) |
| Local feature upsampling | InputLayer | – | – | (1, 8, 1, 8) |
| | Conv3DTr | 1 × 2 × 1 | 1 × 2 × 1 | (1, 8, 2, 8) |
| | Conv3DTr | 1 × 2 × 1 | 1 × 2 × 1 | (1, 8, 4, 8) |
| | Conv3DTr | 1 × 2 × 1 | 1 × 2 × 1 | (1, 8, 8, 8) |
| | Conv3DTr | 1 × 1 × 2 | 1 × 1 × 2 | (1, 8, 8, 16) |
| | Conv3D | 2 × 1 × 1 | 2 × 1 × 1 | (1, 4, 8, 16) |
| | Conv3D | 2 × 2 × 1 | 2 × 2 × 1 | (1, 2, 7, 16) |
| | Conv3D | 1 × 1 × 6 | 1 × 1 × 1 | (1, 2, 7, 11) |
| Core outermost assembly reconstruction task | InputLayer | – | – | (5, 2, 7, 11) |
| | Conv3D | 2 × 5 × 5 | 1 × 1 × 1 | (10, 2, 7, 11) |
| | Conv3D | 2 × 5 × 5 | 1 × 1 × 1 | (16, 2, 7, 11) |
| | Conv3D | 2 × 5 × 5 | 1 × 1 × 1 | (8, 2, 7, 11) |
| | Conv3D | 2 × 5 × 5 | 1 × 1 × 1 | (5, 2, 7, 11) |
| Core neutron field reconstruction task | InputLayer | – | – | (5, 2, 7, 11) |
| | Conv3D | 2 × 5 × 5 | 1 × 1 × 1 | (3, 2, 7, 11) |
| | Conv3D | 2 × 5 × 5 | 1 × 1 × 1 | (4, 2, 7, 11) |
| | Conv3D | 2 × 5 × 5 | 1 × 1 × 1 | (5, 2, 7, 11) |
| | Conv3D | 2 × 5 × 5 | 1 × 1 × 1 | (8, 2, 7, 11) |
| | Conv3D | 2 × 5 × 5 | 1 × 1 × 1 | (8, 2, 7, 11) |
| | Conv3D | 2 × 5 × 5 | 1 × 1 × 1 | (6, 2, 7, 11) |
| | Conv3D | 2 × 5 × 5 | 1 × 1 × 1 | (5, 2, 7, 11) |

$$RD = \frac{|\phi_{\text{reconstructed}} - \phi_{\text{reference}}|}{\phi_{\text{reference}}} \tag{5}$$

where $\phi_{\text{reconstructed}}$ represents the reconstructed data obtained by using the trained model, and $\phi_{\text{reference}}$ represents the neutron flux obtained through Monte Carlo simulations, where the number of particles for the Monte Carlo fixed source simulation was 10^9 .

Based on the calculation results of the above relative deviation, the average relative deviation ARD and maximum relative deviation RD_{max} were used as the evaluation criteria. As there were 460 reconstruction units in this study, taking the average relative deviation as the evaluation criterion will inevitably cover certain of the larger deviations, which will affect the final judgment. Therefore, 10% was selected as the reconstruction deviation threshold, and the reconstruction unit with a relative deviation of more than 10% $RD_{\geq 10\%}$ between the reconstructed value and the Monte Carlo simulation reference value was considered as an additional evaluation criterion.

5.2 Experiments on SCDs

To test the reconstruction effect of DTHNet on SCDs, the core neutron field reconstruction performance was tested on 18 datasets of SCDs, and the reconstruction results were compared with those based on PRA. The statistical results in Table 5 revealed that with the utilization of DTHNet, on average, the RD_{max} was 10.82%, and the number of $RD_{\geq 10\%}$ was 2. When employing PRA, the RD_{max} is 12.39%, and the number of $RD_{\geq 10\%}$ was 3. Meanwhile, the average relative

Table 5 Average result of the evaluation on the SCDs

| PRA | | | DTHNet | | |
|-----------|-----------------------|------------------|-----------|-----------------------|------------------|
| ARD (%) | RD_{max} (%) | $RD_{\geq 10\%}$ | ARD (%) | RD_{max} (%) | $RD_{\geq 10\%}$ |
| 1.22 | 12.39 | 3 | 1.35 | 10.82 | 2 |

PRA Pipeline Reconstruction Architecture, DTHNet Dual-Task Hybrid Network Architecture

deviations ARD of the two methods were slightly different, and both remained within 2.5%.

To facilitate a more intuitive comparison of the reconstruction outcomes of the two architectures, a line chart was generated as shown in Fig. 8. The chart illustrates RD_{max} and $RD_{\geq 10\%}$ for the 18 datasets of SCDs. Upon examination of the chart, it is evident that the reconstruction RD_{max} of PRA was inferior to that of DTHNet on 14 datasets, and the reconstruction $RD_{\geq 10\%}$ of PRA was inferior to that of DTHNet on 11 datasets.

Thus, this analysis indicates that the DTHNet was well suited for core neutron field reconstruction in the case of a

single changed region, and it offered certain advantages over the PRA architecture.

5.3 Experiments on SRMDs and MRMDs

The change in SCDs is relatively simple, and there is only a single changed region in each dataset. To assess the adaptability of DTHNet to complex core changes, we evaluated the core neutron field reconstruction efficacy of this model on both SRMDs and MRMDs.

Table 6 presents the reconstruction effect on SRMDs and MRMDs; compared with the ARD of the reconstructed

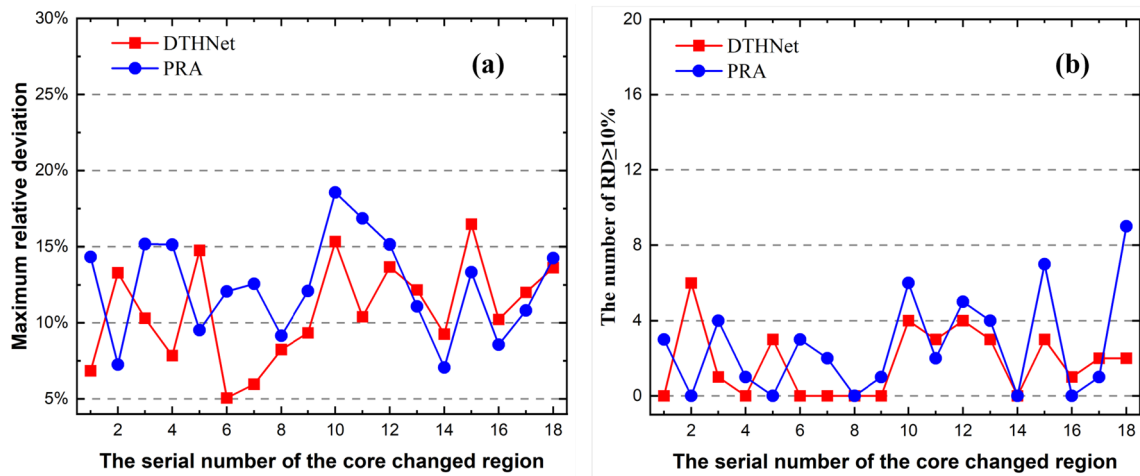


Fig. 8 (Color online) Maximum relative deviation RD_{max} and the number of $RD_{\geq 10\%}$ evaluated by PRA and DTHNet on SCDs

Table 6 Results of the evaluation on the SRMDs and MRMDs; where m is the location uncertainty of a single channel region, and n represents the number of core changed regions

| Dataset serial number | SRMDs | | | | MRMDs | | | |
|-----------------------|-------|-----------|----------------|------------------|-------|-----------|----------------|------------------|
| | m | ARD (%) | RD_{max} (%) | $RD_{\geq 10\%}$ | n | ARD (%) | RD_{max} (%) | $RD_{\geq 10\%}$ |
| 1 | 2 | 1.32 | 7.91 | 0 | 2 | 0.93 | 11.66 | 1 |
| 2 | 3 | 1.20 | 13.15 | 3 | 3 | 1.32 | 17.15 | 6 |
| 3 | 4 | 1.49 | 12.44 | 1 | 4 | 1.07 | 17.28 | 5 |
| 4 | 5 | 0.93 | 7.94 | 0 | 5 | 1.59 | 16.50 | 10 |
| 5 | 6 | 1.15 | 16.17 | 5 | 6 | 1.94 | 18.92 | 15 |
| 6 | 7 | 1.59 | 17.00 | 7 | 7 | 1.47 | 22.54 | 15 |
| 7 | 8 | 1.28 | 14.21 | 5 | 8 | 2.04 | 21.17 | 24 |
| 8 | 9 | 1.24 | 17.49 | 10 | 9 | 1.37 | 20.88 | 22 |
| 9 | 10 | 1.70 | 24.89 | 9 | 10 | 1.89 | 25.88 | 25 |
| 10 | 11 | 1.75 | 17.72 | 10 | 11 | 1.62 | 27.71 | 32 |
| 11 | 12 | 1.95 | 20.00 | 13 | 12 | 1.72 | 20.32 | 34 |
| 12 | 13 | 2.09 | 32.57 | 22 | 13 | 1.94 | 30.71 | 26 |
| 13 | 14 | 2.11 | 27.86 | 23 | 14 | 1.92 | 26.95 | 25 |
| 14 | 15 | 1.85 | 31.61 | 23 | 15 | 1.98 | 40.26 | 22 |
| 15 | 16 | 2.06 | 28.77 | 23 | 16 | 1.78 | 22.47 | 40 |
| 16 | 17 | 2.06 | 37.82 | 28 | 17 | 2.42 | 30.52 | 44 |
| 17 | 18 | 2.01 | 33.72 | 25 | 18 | 1.80 | 28.87 | 38 |

results on SCDs, the ARD on SRMDs and MRMDs increased; however, it could be maintained within 3%. On average, RD_{\max} of SRMDs was 21.25%, and the number of $RD_{\geq 10\%}$ was 12. When the location uncertainty m of a single changed region was small (9), the number of $RD_{\geq 10\%}$ could be maintained to within 10. Meanwhile, on average, RD_{\max} of MRMDs was 22.92%, and the number of $RD_{\geq 10\%}$ was 23. When the number of changed regions n in a dataset was less than five, $RD_{\geq 10\%}$ was maintained within 10. The results show that DTHNet can achieve core neutron field reconstruction on some datasets of SRMDs and MRMDs, further proving the applicability of the architecture for neutron field reconstruction under complex core changes.

To more intuitively analyze the reconstruction effect of DTHNet under complex core changes. A line chart is drawn for the data in Table 6, as shown in Fig. 9. It displays the RD_{\max} and maximum number of $RD_{\geq 10\%}$ values of the reconstruction results for SRMDs and MRMDs, respectively. As depicted in Fig. 9a, the reconstruction deviation increased with location uncertainty of single changed region. Similarly, when a larger number of regions underwent changes, as shown in Fig. 9b, the efficacy of the reconstruction diminished. These results indicate that the location uncertainty of a single core-changed region and the number of core-changed regions at a certain time significantly impact the reconstruction effect of DTHNet. Therefore, the continuous improvement of the network architecture of the DTHNet method and further enhancement of its applicability under various complex changes in the core will be the focus of subsequent research.

5.4 Experiment on noise data

To verify the effect of neutron field reconstruction in the case of signals containing noise, reconstruction experiments were performed wherein the ex-core detection signals were

affected by noise. When the location uncertainty m of a single changed region did not exceed nine, and the number of multiple changed regions n did not exceed five, the ex-core detection signals were disturbed by noise to obtain noisy data ($SRMDs_{\text{noise}}$ and $MRMDs_{\text{noise}}$). Noise generation is based on the inherent error of the detector, which ranges as $\pm 20\%$ – $\pm 30\%$ in current engineering applications. The process of adding noise is as follows. First, six interference intervals ($\pm 2\%$, $\pm 5\%$, $\pm 10\%$, $\pm 15\%$, $\pm 20\%$ and $\pm 25\%$) for the ex-core detection are set, and then the $SRMDs_{\text{noise}}$ and $MRMDs_{\text{noise}}$ are generated by adding noise to each detection signal of $SRMDs_{(n \leq 9)}$ and $MRMDs_{(m \leq 5)}$.

The DTHNet method was trained and tested based on the acquired noise data. Table 7 presents the results of the reconstruction using the noise data. Compared with the results presented in Table 6, for $SRMDs_{\text{noise}}$, when the degree of interference was $\pm 2\%$, on average, ARD increased by approximately 0.22%, RD_{\max} increased by approximately 8.33%, and among the 460 reconstructed units, the number of $RD_{\geq 10\%}$ increased by approximately 6. However, the reconstruction accuracy decreased sharply as the degree of interference increased. For $MRMDs_{\text{noise}}$, when the degree of interference was $\pm 2\%$, among the 460 reconstructed units, although the average number of $RD_{\geq 10\%}$ increased by approximately six, the average ARD increased by approximately 0.23%. Further, the average RD_{\max} increased by approximately 5.05%. As the degree of interference continued to increase, the reconstructed ARD and RD_{\max} did not change significantly, and only the average number of $RD_{\geq 10\%}$ increased. Thus, when the ex-core detection signals were noisy, the location uncertainty of the core change had a significant impact on the accuracy of the reconstruction; however, an increase in the number of changed regions had a slight impact on the reconstruction accuracy of the method.

In summary, when the noise interference amplitude is within $\pm 2\%$, the DTHNet method can accurately and stably

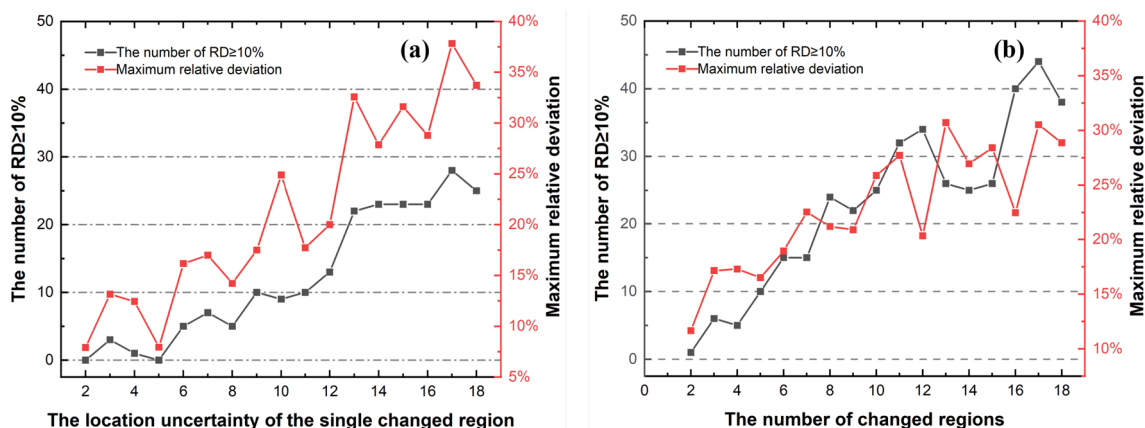


Fig. 9 (Color online) RD_{\max} for each dataset on the SRMDs and MRMDs. The m value of SRMDs and n value of MRMDs increase linearly with the serial number of dataset

Table 7 Average result on SRMDs_{noise} and MRMDs_{noise}

| The degree of interference | SRMDs _{noise} | | | MRMDs _{noise} | | |
|----------------------------|------------------------|-----------------------|--------------------|------------------------|-----------------------|--------------------|
| | ARD (%) | RD _{max} (%) | RD _{≥10%} | ARD (%) | RD _{max} (%) | RD _{≥10%} |
| ±2% | 1.49 | 21.62 | 16 | 1.60 | 21.14 | 16 |
| ±5% | 1.69 | 83.02 | 35 | 1.74 | 22.85 | 22 |
| ±10% | 2.04 | 129.19 | 75 | 1.72 | 21.22 | 27 |
| ±15% | 2.18 | 162.77 | 67 | 1.87 | 25.02 | 28 |
| ±20% | 2.34 | 168.14 | 73 | 2.12 | 22.86 | 40 |
| ±25% | 2.25 | 161.97 | 76 | 2.24 | 26.95 | 45 |

Table 8 Average result of the ablation experiments on SCDs, SRMDs and MRMDs

| Database | Architecture | ARD (%) | RD _{max} (%) | RD _{≥10%} |
|----------|------------------------|---------|-----------------------|--------------------|
| SCDs | DTHNet | 1.35 | 10.82 | 1.78 |
| | DTHNet(without Task A) | 1.35 | 13.39 | 4.72 |
| | DTHNet(without GLFS) | 5.15 | 100 | 37.60 |
| SRMDs | DTHNet | 1.63 | 21.25 | 12.17 |
| | DTHNet(without Task A) | 1.86 | 24.24 | 14.31 |
| | DTHNet(without GLFS) | 7.41 | 102 | 49.37 |
| MRMDs | DTHNet | 1.69 | 22.92 | 22.82 |
| | DTHNet(without Task A) | 2.08 | 25.21 | 43.47 |
| | DTHNet(without GLFS) | 4.10 | 99.16 | 56.94 |

reconstruct most neutron fields. Subsequently, we will continue to optimize the reconstruction method under noise interference to improve the stability of neutron field off situ reconstruction methods.

5.5 Reconstruction time

To test the reconstruction speed of the proposed method, the time required for model training and reconstruction (experimental environment: windows11+NVIDIA 2080Ti) was determined. The model was trained for approximately 3333 s on each dataset, and the results of neutron field reconstruction could theoretically be obtained in approximately 3 s. Therefore, it can be considered that this method satisfies the real-time monitoring requirements for the neutron field.

5.6 Ablation study

By analyzing the aforementioned experimental effect, it is evident that DTHNet exhibits superiority not only in comparison to PRA under a single-region change, but also in its capacity to achieve precise reconstruction under some complex core changes. To further validate the effectiveness of the method design, ablation experiments were conducted on a global-local feature upsampling module and dual-task training. The results are presented in Table 8.

To assign the features of the ex-core detection signals to each reconstruction unit to improve the overall reconstruction accuracy, DTHNet incorporates a global-local feature upsampling module. To validate the efficacy of this module, we conducted ablation experiments, the results of which are presented in Table 8.

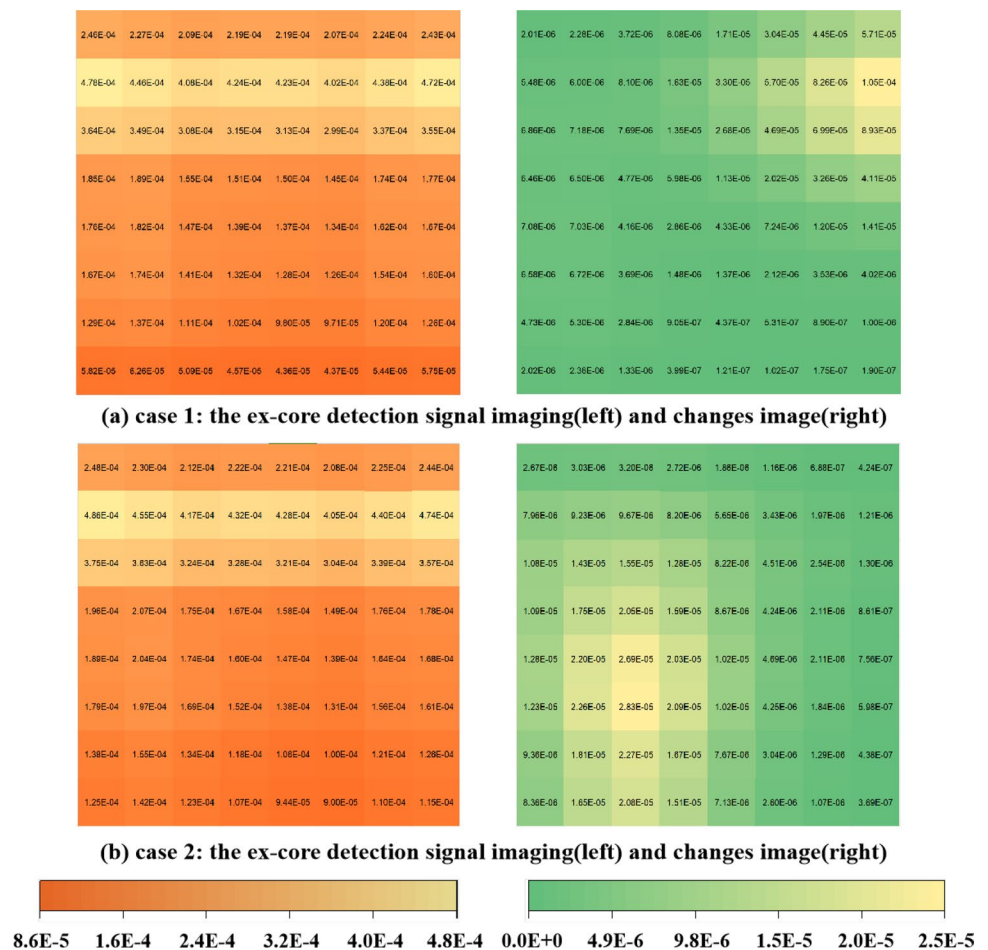
When the global-local feature upsampling module was replaced by a common upsampling module, the average RD_{max} on SCDs, SRMDs, and MRMDs was approximately 89%, 81%, and 74%, respectively. In addition, the average number of RD_{≥10%} in SCDs, SRMDs, and MRMDs increased significantly. From this observation, it is evident that global-local feature upsampling captures ex-core detection information and enhances the core reconstruction efficiency.

In DTHNet, the reconstruction task of neutron field in the outermost core assemblies (Task A) was used to assist the core neutron field reconstruction task (Task B). To verify the assistance effect of Task A, core neutron field reconstruction experiments were performed after Task A was removed. Comparing the results of DTHNet and DTHNet (without Task A) in Table 8, it can be observed that ARD increased slightly for SCDs, SRMDs, and MRMDs. In addition, the average RD_{max} values of the SCDs, SRMDs, and MRMDs were approximately 2.57%, 2.99%, and 2.29%, respectively. The average number of RD_{≥10%} increased by 2 ~ 3 for SCDs and SRMDs but increased significantly for MRMDs. These results show that the reconstruction task of the neutron field in the outermost core assemblies improved the accuracy of core neutron field reconstruction.

5.7 Error analysis

To further analyze the details of the model prediction, two cases of core changes were randomly selected, and the ex-core detection signals of the two cases were simulated using the Monte Carlo transport program. The neutron flux distribution of the core assembly calculated by Monte Carlo transport was used as the reference data to evaluate the reconstruction effect. Figure 10 shows the two types of the ex-core detection signals and their changes compared to the

Fig. 10 (Color online) Visualization of two ex-core detection signals. The change image indicates that the upper of the core has changed under case1, and the lower of the core has changed under case2



initial signals. The upper part of the core assembly changed in case1, and the lower part of the core changed in case2.

In this section, we analyze the reconstruction effect of the neutron flux distribution of the core assembly and the distribution of the reconstruction deviation. According to the reconstruction evaluation criteria in Sect. 5.1, the relative deviation RD between the reconstructed and reference neutron fluxes was calculated, and the errors were analyzed based on RD . Figures 11 and 12 show RD visualizations of core neutron flux reconstruction when two and four regions of the core changed, respectively.

In Figs. 11 and 12, the bold part of the frame line indicates the changed regions. The assemblies with large errors were mainly concentrated in the core-changed regions and $[1.00, 2.00 \times 10^1]$ MeV. Therefore, it can be concluded that the large error in certain assemblies was related to the spatial position and energy group.

First, the spatial influencing factors were analyzed. Figures 11f and 12f show that the reconstruction error of the changed regions was generally greater than that of the unchanged regions. The reasons are as follows. This study provided the model with sufficient pairs of ex-core detection signals and in-core neutron field data, and the model

was trained to learn some nonlinear relationship between the ex-core detection signals and each unit to be reconstructed. However, in the learning process, if the change in the amplitude of the unit to be reconstructed is uncertain, then it is difficult for the model to learn the exact nonlinear relationship between the ex-core detection signals and the value of the reconstruction unit. According to the dataset settings in Sect. 4.1, the diversity of the neutron field change amplitude was increased to simulate the uncertainty of the core change during the reactor operation. Thus, even if any two samples of the training set consistently changed their regions, the magnitude of the change was inconsistent. Thus, when the changed and unchanged regions were trained synchronously, it was difficult to fit the nonlinear relationship between the changed regions of the core and ex-core detection signals, which is the primary cause of the uneven distribution of the error space.

Next, the energy-influencing factors were analyzed. This study mainly selected the RD of the reconstruction unit in the $[0, 1.00 \times 10^{-2}]$ MeV, $[1.00 \times 10^{-2}, 1.00 \times 10^{-1}]$ MeV and $[1.00, 2.00 \times 10^1]$ MeV with obvious error distribution for visualization. As evident from the two figures, the RD was within 13%, the number of $RD_{\geq 10\%}$ did

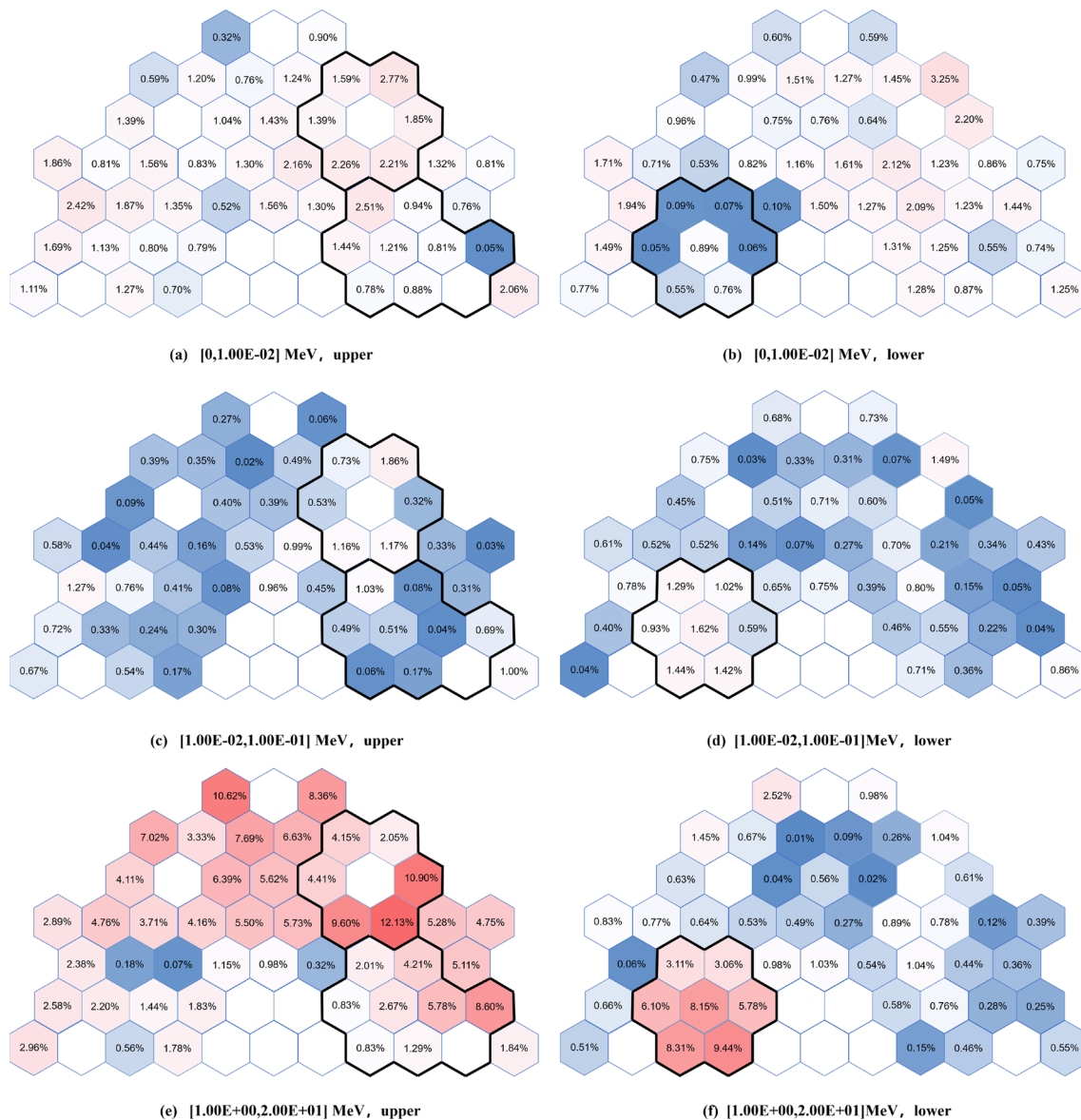


Fig. 11 (Color online) *RD* of certain core reconstruction units under case1. The redder the color, the larger the *RD*; and the bluer the color, the smaller the *RD*

not exceed 3, but the *RD* distribution of $[0, 1.00 \times 10^{-2}]$ MeV and $[1.00, 2.00 \times 10^1]$ MeV exceeded that of $[1.00 \times 10^{-2}, 1.00 \times 10^{-1}]$ MeV. This is because if the magnitude of the values is different among reconstruction units, neural network models may struggle to learn suitable weights and biases for each reconstruction unit simultaneously, such that the individual reconstruction units cannot obtain the optimal results at the same time. Because this study is focused a fast neutron reactor, the distribution of neutrons among the five energy groups is uneven; therefore, error distribution between different energy groups is inevitable.

In summary, the errors of some reconstruction units may be affected by both spatial and energy factors. The design of the method will be further improved according to the above analysis to improve the accuracy of the reconstruction under complex changes in neutron fields.

6 Conclusion

This study proposed a novel reconstruction architecture, DTHNet, based on multitasking deep learning. Based on the PRA method, the outermost assembly and core neutron field reconstruction tasks were jointly trained. In addition,

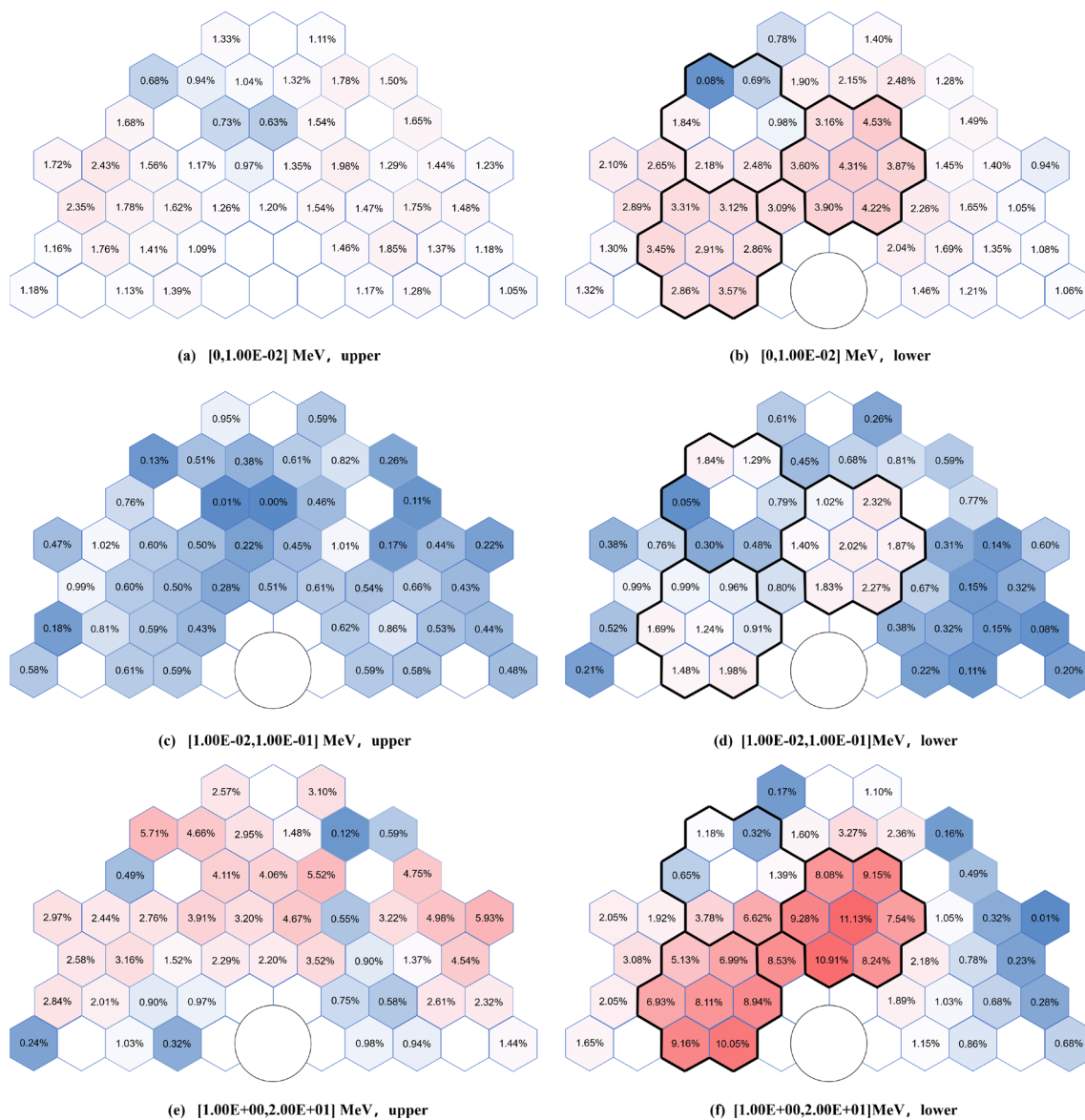


Fig. 12 (Color online) *RD* of certain core reconstruction units under case2. The redder the color, the larger the *RD*; and the bluer the color, the smaller the *RD*

to fully extract the features of the ex-core detection signals, this study designed a global-local feature upsampling module which assigns and the information to the high- and low-energy groups, respectively, from the ex-core detection signals. Further, the upsampled features were used for the training of the two downstream tasks. To verify the validity and applicability of the proposed method for core neutron field reconstruction, DTHNet was tested on SCDs, SRMDs, and MRMDs. The results demonstrated that when the location uncertainty of a single region did not exceed nine and the number of multiple changed regions did not exceed five. Further, the effect of the dual-task hybrid reconstruction architecture had a certain

applicability under certain complex core changes. When the noise interference amplitude was within $\pm 2\%$, the DTHNet method could accurately and stably reconstruct most of the neutron fields. In summary, this study offers a new technological pathway for the accurate monitoring of reactor cores. According to the experimental results, the continuous improvement of the network architecture of the DTHNet method and further enhancement of its applicability under various complex core changes will be the focus of subsequent research. Based on this, we will optimize the reconstruction method under noise interference to improve the accuracy and stability of neutron field off situ reconstruction methods.

Author Contributions All authors contributed to the study conception and design. Material preparation, data collection and analysis were performed by Pei Cao, Guo-Min Sun and Zi-Hui Yang. The first draft of the manuscript was written by Pei Cao and all authors commented on previous versions of the manuscript. All authors read and approved the final manuscript.

Data Availability Statement The data that support the findings of this study are openly available in Science Data Bank at <https://cstr.cn/31253.11.sciencedb.j00186.00231> and <https://www.doi.org/10.57760/sciencedb.j00186.00231>.

Declarations

Conflict of interest The authors declare that they have no Conflict of interest.

References

1. I. Meesha, M. Rae, W. Irene, Peoples' perception th nuclear energy. *Energies* **15**, 4397 (2022). <https://doi.org/10.3390/en15124397>
2. Q. Zhang, B. Deng, X. Liu et al., Deconvolution-based real-time neutron flux reconstruction for self-powered neutron detector. *Nucl. Eng. Des.* **326**, 261–267 (2018). <https://doi.org/10.1016/j.nucengdes.2017.11.024>
3. I. Ramezani, M.B. Ghofrani, Reconstruction of neutron flux distribution by nodal synthesis method using online in-core neutron detector readings. *Prog. Nucl. Energy* **131**, 103574 (2021). <https://doi.org/10.1016/j.pnucene.2020.103574>
4. B. Anupreethi, V.S. Yellapu, A. Gupta et al., Performance evaluation of AHWR flux mapping system during normal operational scenarios. *Nucl. Eng. Des.* **390**, 111686 (2022). <https://doi.org/10.1016/j.nucengdes.2022.111686>
5. S. Liu, Z. Shao, Y. Sang et al., A general method for delay compensation of self-powered neutron detectors in reactors. *Ann. Nucl. Energy* **193**, 110035 (2023). <https://doi.org/10.1016/j.anuce.2023.110035>
6. Y. Zhang, X. Fang, S. Jiang et al., The direct measurement of HTR-10 in-core neutron flux. *Nucl. Eng. Des.* **401**, 112085 (2023). <https://doi.org/10.1016/j.nucengdes.2022.112085>
7. L.E. Moloko, P.M. Bokov, X. Wu et al., Prediction and uncertainty quantification of Safari-1 axial neutron flux profiles with neural networks. *Ann. Nucl. Energy* **188**, 109813 (2023). <https://doi.org/10.1016/j.anucene.2023.109813>
8. X. Zhao, Y. Zou, R. Yan et al., Analysis of burnup performance and temperature coefficient for a small modular molten salt reactor started with plutonium. *Nucl. Sci. Tech.* **34**, 17 (2023). <https://doi.org/10.1007/s41365-022-01155-2>
9. Y. Wu, *Comprehensive neutronics simulations* (Springer, Singapore, 2019), pp.375–375. <https://doi.org/10.1007/978-981-13-6520-1>
10. B. Yan, C. Wang, L. Li, The technology of micro heat pipe cooled reactor: a review. *Ann. Nucl. Energy* **135**, 106948 (2020). <https://doi.org/10.1016/j.anucene.2019.106948>
11. X. Wang, F. Zhao, Y. He et al., Development and verification of helium-xenon mixture cooled small reaction system. *Prog. Nucl. Energy* **160**, 104679 (2023). <https://doi.org/10.1016/j.pnucene.2023.104679>
12. P. Lien, U. Rohatgi, Scaling challenges in small modular reactor. *Nucl. Eng. Des.* **407**, 112309 (2023). <https://doi.org/10.1016/j.nucengdes.2023.112309>
13. Q. Gan, P. Cao, An inversion method of in-core neutron field based on ex-core neutron spectrum measurement. *Nucl. Tech.* (in Chinese) **42**, 090502 (2019). <https://doi.org/10.11889/j.0253-3219.2019.hjs.42.090502>
14. S. Zhu, S. Zhuang, S. Fang et al., 3-D gamma radiation field reconstruction method using limited measurements for multiple radioactive sources. *Ann. Nucl. Energy* **175**, 109247 (2022). <https://doi.org/10.1016/j.anucene.2022.109247>
15. M. Ugoletti, M. Agostini, Development of the tomographic reconstruction technique of spider negative ion beam. *Fusion Eng. Des.* **189**, 113470 (2023). <https://doi.org/10.1016/j.fusengdes.2023.113470>
16. R. Kimura, Y. Nakai, S. Wada, Reactor core power distribution reconstruction method by ex-core detectors based on the correlation effect between fuel regions. *Nucl. Sci. Eng.* **195**, 1–12 (2021). <https://doi.org/10.1080/00295639.2021.1908081>
17. R. Kimura, Y. Nakai, T. Sano et al., Time-dependent experiment on reactor power distribution estimation by ex-core detectors at UTR-KINKI. *Nucl. Technol.* **209**, 1859–1866 (2023). <https://doi.org/10.1080/00295450.2023.2212828>
18. R. Rodionov, G. Nemtcev, A. Krasilnikov, Fusion neutron emissivity tomography for ITER vertical neutron camera. *Nucl. Instrum. Methods Phys. Res. Sect. A* **1040**, 167127 (2022). <https://doi.org/10.1016/j.nima.2022.167127>
19. G. Tanja, K. Bor, A. Klemen et al., Determination of neutron flux redistribution factors for a typical pressurized water reactor ex-core measurements using monte carlo technique. *Front. Energy Res.* **11**, 1137867 (2023). <https://doi.org/10.3389/fenrg.2023.1137867>
20. X. Peng, Q. Li, K. Wang, Core axial power shape reconstruction based on radial basis function neural network. *Ann. Nucl. Energy* **73**, 339–344 (2014). <https://doi.org/10.1016/j.anucene.2014.06.055>
21. W. Li, P. Ding, W. Xia et al., Artificial neural network reconstructs core power distribution. *Nucl. Eng. Technol.* **54**, 617–626 (2022). <https://doi.org/10.1016/j.net.2021.08.015>
22. J. Bae, T. Wu, J. Igor, Reconstruction of fast neutron direction in segmented organic detectors using deep learning. *Nucl. Instrum. Methods Phys. Res. Sect. A* **1049**, 168024 (2023). <https://doi.org/10.1016/j.nima.2023.168024>
23. Y. Yao, J. Wang, M. Xie, Adaptive residual CNN-based fault detection and diagnosis system of small modular reactors. *Appl. Soft Comput.* **114**, 108064 (2022). <https://doi.org/10.1016/j.asoc.2021.108064>
24. B. Salmassian, A. Rabiee, M.R. Nematollahi et al., Diagnosing core local flow blockages in a VVER-1000/446 reactor using ex-core detectors and neural networks. *Prog. Nucl. Energy* **161**, 104736 (2023). <https://doi.org/10.1016/j.pnucene.2023.104736>
25. Y. Ling, T. Huang, Q. Yue et al., Improving the estimation accuracy of multi-nuclide source term estimation method for severe nuclear accidents using temporal convolutional network optimized by bayesian optimization and hyperband. *J. Environ. Radioact.* **242**, 106787 (2022). <https://doi.org/10.1016/j.jenvrad.2021.106787>
26. C. Victor, M. Elia, P. Roberto et al., Convolutional neural network-aided temperature field reconstruction: an innovative method for advanced reactor monitoring. *Nucl. Technol.* **209**, 1–22 (2023). <https://doi.org/10.1080/00295450.2022.2151822>
27. J. Liu, H. Jiang, Z. Cui et al., Simultaneous measurement of energy spectrum and fluence of neutrons using a diamond detector. *Sci. Rep.* **12**, 12022 (2022). <https://doi.org/10.1038/s41598-022-16235-x>
28. Y. Hao, Z. Wu, Y. Pu et al., Research on inversion method for complex source-term distributions based on deep neural networks. *Nucl. Sci. Tech.* **34**, 195 (2023). <https://doi.org/10.1007/s41365-023-01327-8>

29. X. Wei, S. Sun, W. Tang et al., Reconstruction of tokamak plasma safety factor profile using deep learning. *Nucl. Fusion* **63**, 086020 (2023). <https://doi.org/10.1088/1741-4326/acdf00>
30. J. Seo, S. Kim, A. Jalalvand, Avoiding fusion plasma tearing instability with deep reinforcement learning. *Nature* **626**, 746–751 (2024). <https://doi.org/10.1038/s41586-024-07024-9>
31. P. Cao, Q. Gan, J. Song et al., An artificial neural network based neutron field reconstruction method for reactor. *Ann. Nucl. Energy* **138**, 107195 (2020). <https://doi.org/10.1016/j.anucene.2019.107195>
32. P. Cao, Q. Gan, A neutron field reconstruction method for reactor based on semi-supervised learning. *Ann. Nucl. Energy* **152**, 108020 (2021). <https://doi.org/10.1016/j.anucene.2020.108020>
33. P. Cao, C. Cao, Q. Gan, A 3-D neutron distribution reconstruction method based on the off-situ measurement for reactor. *IEEE Trans. Nucl. Sci.* **68**, 2694–2701 (2021). <https://doi.org/10.1109/TNS.2021.3123381>
34. J. Zhao, W. Lv, B. Du et al., Deep multi-task learning with flexible and compact architecture search. *Int. J. Data Sci. Anal.* **15**, 187–199 (2021). <https://doi.org/10.1007/s41060-021-00274-0>
35. Y. Zhao, X. Wang, T. Che et al., Multi-task deep learning for medical image computing and analysis: a review. *Comput. Biol. Med.* **153**, 106496 (2023). <https://doi.org/10.1016/j.combiomed.2022.106496>
36. Y. Wu, Y. Bai, Y. Song et al., Development strategy and conceptual design of China lead-based research reactor. *Ann. Nucl. Energy* **87**, 511–516 (2016). <https://doi.org/10.1016/j.anucene.2015.08.015>

Springer Nature or its licensor (e.g. a society or other partner) holds exclusive rights to this article under a publishing agreement with the author(s) or other rightsholder(s); author self-archiving of the accepted manuscript version of this article is solely governed by the terms of such publishing agreement and applicable law.